Transparent high-strength nanosized yttria stabilized zirconia obtained by pressure-less sintering

Omid Akhlaghi, Erik Camposilvan, Zahra Goharibajestani, Sirous Khabbaz Abkenar, Cleva Ow-Yang, Yves Jorand, Laurent Gremillard, V. Garnier, Jérôme Chevalier

To cite this version:

Omid Akhlaghi, Erik Camposilvan, Zahra Goharibajestani, Sirous Khabbaz Abkenar, Cleva Ow-Yang, et al.. Transparent high-strength nanosized yttria stabilized zirconia obtained by pressure-less sintering. Journal of the European Ceramic Society, 2022, 42 (15), pp.7187-7195. 10.1016/j.jeurceramsoc.2022.07.027 . hal-03786754

HAL Id: hal-03786754
https://hal.science/hal-03786754v1

Submitted on 7 Mar 2023

Transparent high-strength nanosized yttria stabilized zirconia obtained by pressure-less sintering

Published in Journal of the European Ceramic Society 42[15] pp. 7187-95 (2022)
https://doi.org/10.1016/j.jeurceramsoc.2022.07.027

M. Akhlaghi[a], E. Camposilvan[b], Z. Goharibajestani[c], S. Khabbaz Abkenar[d,e], C.W. Ow-Yang[d,e], Y. Jorand[a], L. Gremillard[a], V. Garnier[a], J. Chevalier[a,*]

[a] Université de Lyon, INSA-Lyon, CNRS, MATEIS UMR5510, 7 Av. Jean Capelle, F-69621 Villeurbanne Cedex, France.
[b] Mathym SAS, Champagne-au-Mont-d'Or, France
[c] University of Le Mans, IMMM, Avenue Olivier Messiaen, 72085 Le Mans, France
[d] Materials Science & Nano-Engineering Program, Sabanci University, Tuzla, Istanbul 34956, Turkey
[e] Nanotechnology Research and Application Center (SUNUM), Sabanci University, Tuzla, Istanbul 34956, Turkey

* Corresponding author: Jerome.chevalier@insa-lyon.fr

Keywords

Yttria stabilized zirconia; Pressure-less sintering; Nanograin; Transparent ceramics

Abstract

This work describes the development of transparent high-strength Yttria-Stabilized Zirconia (YSZ) ceramics with ultra-fine grain size utilizing conventional pressure-less densification. Starting with nanoparticles with diameter < 10 nm, it was possible to achieve full densification (>99.5% of theoretical density) at a sintering temperature of 1100–1200 °C. The average grain size of the resulting dense ceramics was 75 nm in 3 mol. % YSZ and 85 nm in 8 mol. % YSZ, showing in-line light transmission of 38% and 51% at a wavelength of 800 nm and average biaxial strength (piston on three balls test on samples of diameter 12 mm and thickness 1 mm) of 1980 MPa and 680 MPa, respectively. The nano-grained structure, absence of color centers, and miniaturization of residual pores enable the excellent light transmission. The high biaxial strength is attributed to the refined microstructure, but also to the martensitic tetragonal-to-monoclinic phase transformation that remains active even in nano-sized zirconia grains.

1. Introduction

Polycrystalline transparent ceramics are of great interest due to their unique combination of physical, mechanical, and optical properties. These high performance materials enable variety of applications such as infrared (IR) and heat resistant windows [1], lasers [2], [3], ballistic armors [4] etc. Fabrication of transparent ceramics generally requires high temperatures and long densification times to eliminate residual pores as the main light scattering centers. Light scattering is a function of pore size and content and depends on the wavelength [5]. Consolidation conditions give rise to grain growth which also favors transparency but at the expense of the mechanical properties [1]. Recent findings revealed that the scattering efficiency of residual pores substantially declines with size in nano-range [6], [7]. As grain boundaries have less impact on transparency of ceramics compared to residual porosity [4], [8], reducing the grain size of polycrystalline ceramics to < 100 nm and consequently, miniaturization of the residual pores can provide simultaneous transparency and higher mechanical performance compared to micron grain-sized counterparts [9], [10].

Yttria Stabilized Zirconia (YSZ) can be the material of choice for the fabrication of nanocrystalline transparent ceramics. YSZ has attracted considerable attention in a promise of merging, in a single system, materials with outstanding mechanical properties (i.e. 3 mol. % YSZ with a strength of more than 900 MPa and fracture toughness of 5–10 MPa·m$^{1/2}$) and others with optical transparency (i.e. 8 mol. % YSZ) [11], [12], [13]. 3 mol.% YSZ has been predominantly an opaque material mainly due to birefringence of the tetragonal phase and thus, optical anisotropy at the grain boundaries [14]. On the other hand, 8YSZ—fully cubic zirconia offers an isotropic refractive index, which promotes transparency, but the absence of the stress-induced phase transformation in cubic zirconia significantly lowers the mechanical properties of 8YSZ (i.e., <400 MPa and <1.5 MPa·m$^{1/2}$) [9]. Currently, consolidation of ceramic powders to nano-crystalline transparent structures can be achieved only by high-pressure (e.g., 1 GPa) sintering methods such as hot isostatic pressing (HIP) or spark plasma sintering (SPS) [15], [16]. Zhang et al. [17] and Klimke et al. [4] have shown an increase of transparency with YSZ of ~100 nm grain size consolidated by SPS and HIP, respectively. Anselmi et al. [18] further demonstrated the feasibility of 20% and 50% Real In-line Transmission (RIT) in the visible range (*i.e.*, wavelength of 400–800 nm) for 3YSZ and 8YSZ, respectively, through obtaining fully-dense structures (thickness of 1 mm) with grain size of 50 nm after SPS and annealing in air. However, color centers and residual carbon generated by the reducing environment [11], as well as production cost, limited product size, and essential post-sintering annealing [19], [20], raise questions about practicality of such non-conventional consolidation methods in commercial production [21].

Given the limitations of the high-pressure sintering methods, using conventional pressure-less sintering is obviously preferable for densification of ceramics. In this approach, size and distribution of residual pores in dense bodies are directly influenced by powder features and green body preparation [22], [23]. With the goal of obtaining crack-free transparent bulk ceramics with a final grain size of less than 100 nm, the initial nanopowders should have a much smaller particle size. Under these circumstances, controlling the powder characteristics (e.g. size and agglomeration), green body formation (e.g., density, pore size, and pore size distribution), and sintering process becomes quite challenging. No such material has been obtained by pressure-less sintering so far.

In this study, 1.5–8 mol. % YSZ green bodies obtained from optimized nano-dispersions with an average primary particle size of 8 nm were characterized and densified by conventional pressure-less sintering in air. As reliable experimental data on both transparency and mechanical properties of nano-crystalline YSZ are scarce, we focused on the effect of microstructure on both optical properties (real in-line and total forward transmission) and mechanical performance (biaxial strength, hardness and fracture toughness) of nano-crystalline YSZ ceramics.

2. Experimental section

2.1. Starting materials and sample preparation

Aqueous colloidal suspensions of yttria-doped zirconia nanoparticles were prepared by Mathym SAS (Champagne-au-Mont-d'Or, France). In a typical synthesis, an aqueous solution of a zirconyl chloride octahydrate ($ZrOCl_2.8\ H_2O$, 0.471 M) and yttrium chloride hexahydrate ($YCl_3.6\ H2O$, 0.033 M) were prepared, mixed for 1 h, and the mixed hydroxides were precipitated in an ammonium hydroxide solution (NH_4OH, 3 M). After agitating for 1 h to break soft agglomerates, the resulting hydroxides were kept uninterrupted for 5 min to separate out the sediments. The supernatant was replaced by deionized water until a constant conductivity was achieved (displacement washing, typically 7 times). Subsequently, tetramethylammonium hydroxide pentahydrate solution (TMAOH, 10%) was added dropwise and the mixture was placed into a modified hydrothermal vessel with a Teflon lining and equipped with a propeller. Heat treatment was applied at 200 °C for 1 h under propeller rotation of 180 rpm and 10–12 bar pressure. Fig. S1 shows the particle size and particle size distribution, measured by digital image analysis, of the nanoparticles present in the initial dispersions, indicating an average particle size of 8 ± 1 nm.

After cooling down the hydrothermal vessel, triammonium citrate and polyvinyl alcohol based binder were added to the batch. After homogenization by bath sonication for 2 h, pressure filtration was applied at 10–80 bar over a Whatman Cyclopore polycarbonate membrane with pore size of 100 nm to obtain wet bodies, followed by demolding at humidity-controlled home-made green house (90% relative humidity) and drying in humidity controlled chamber at a rate of 15% humidity decrease per day to reach ambient condition.

The green bodies (Fig. S2) were ground by sandpaper (Grit 400–800) to reduce the thickness to 3 mm and characterized in terms of apparent density and pore size. The samples were then debinded at 600 °C for 2 h (with temperature ramp of 0.5 °C/min), and finally densified: 1.5–2YSZ at 1100 °C for 2 h, 3YSZ at 1150 °C for 2 h, and 4–8YSZ at 1200 °C for 1 h. Heating and cooling rates at this stage were fixed at 3 °C/min for all samples. All sintered samples were ground to 1 mm thickness with 120–1200 grit paper and then mirror-polished with diamond pastes down to 1-µm for further characterizations.

Some of 3YSZ green bodies were used for Hot Isostatic Pressing (HIP, Type ASEA pressure systems Model N°QIH3 with graphite chamber) for comparison. To keep grain growth at minimum, green body discs with 3 mm thickness were pre-sintered in air at 950 °C for 1 h at a rate of 10 °C/min. The material was then subjected to HIP at 1100 °C under argon atmosphere and a pressure of 200 MPa for 10 h.

2.2. Methods

Light transmission measurements were conducted in a Jasco V-670 UV-Visible/NIR spectrophotometer using standard illuminant D65 on samples of 1 mm thickness. The spectrophotometer was also equipped with a 60 mm integrating sphere for total forward transmission measurement. The transparency was determined in the center of the pellet (spot size 5 mm). RIT measurements were conducted using a shield with an appropriate aperture placed between the sample and the detector to avoid scattered light with angle > 0.5°, and the distance between the sample and the detector was ~1 m.

Biaxial strength was measured with a piston-on-three-balls fixture (universal electromechanical testing machine–Instron 8563), according to ISO 6872 recommendations on the testing procedure, using 10–20 samples per group with diameter of 12.0 ± 0.5 mm and thickness of 1.00 ± 0.02 mm. Few samples were slightly smaller than the ISO 6872 specifications on dimensions (e.g. 11.5 mm in diameter or 0.98 mm in thickness).

Hardness and indentation fracture toughness tests were performed using a Vickers indenter (Vickers hardness tester FV-700) and an applied load of 3 kg for cubic and 10 kg for tetragonal YSZ samples. Results were reported as the average of at least 30 measurements from three different samples. The K_{IC} values were estimated from the formula proposed by Anstis [24] as $0.016 \times \frac{F}{c^{3/2}} \times \left(\frac{E}{H_V}\right)^{3/2}$, where E is Young modulus (210 GPa), F is load (N), H_v is hardness (GPa), and c is half length of the crack generated by indentation (m). It is understood that K_{IC} measured by this technique and calculated from the Anstis equation are only estimations and should rather be considered as 'indentation crack resistance' and not 'real toughness' (Single Edge Notched Beam tests should be preferred). However, we were limited by the size of our samples and we used the values mostly for comparison purposes. Standard 3YSZ (Future-Tech, Japan) with average grain size 0.4 µm was used as a reference, showing a calculated H_v of 12.8 ± 0.3 GPa and K_{IC} of 3.9 ± 0.2 $\text{MPa}\cdot\text{m}^{1/2}$.

SEM observations were conducted on Zeiss Supra 55VP field emission scanning electron microscope, without gold-coating, at acceleration voltage of 1 KeV and working distance of 1 mm. To measure the size of grains, all mirror-polished specimens were further polished by vibratory polishing machine (Vibromet Buehler) for 12 h with a super finishing colloidal silica suspension (0.03 µm, Presi-SPM). To analyze the vicinity of cracks, Vickers indentation was applied on the selected vibratory polished specimens before SEM observation.

X-Ray Diffraction (XRD) patterns were collected by a Bruker AXS diffractometer (Cu Kα– 0.154 nm). The content and composition of cubic and tetragonal phases were calculated by Rietveld analysis via the software Topas 4.0.

The Brunauer-Emmett-Teller (BET) specific surface (SBET) and Barrett-Joyner-Halenda (BJH) profile were determined on the green bodies before and after thermal treatment at different temperatures by analyzing the standard nitrogen sorption isotherms at 77 K using a surface area and porosity analyzer (TriStar II 3020, Micrometrics). All samples were dried at 120 °C for 12 h under vacuum prior to the measurement.

Dilatometry analysis was performed on green bodies from room temperature up to 1300 °C using a Setsys evolution–Setaram thermo-mechanical analysis platform with heating rate of 1 °C/min.

The density of dried and sintered samples was measured according to the Archimedes principle in deionized water using MettlerToledoAE100 balance equipped with density determination kit at 25 ± 1 °C. Green bodies were coated by a thin layer of acrylate base adhesive before the measurement.

Thermogravimetric analysis combined with micro gas chromatography and mass spectrometry was conducted on Mettler Toledo TGA-DSC2-µGC operating over a temperature range from 25 °C to 1200 °C with heating rate of 5 °C/min. The emitted gas molecules were separated by molecular sieve (OV1 and Poraplot U columns) and identified by the mass spectrometer.

Electron Energy Loss Spectroscopy (EELS) measurements were performed by using a post-column energy filter spectrometer (Gatan GIF Quantum ER) attached to a spherical aberration-corrected scanning transmission electron microscope (JEM-ARM 200CF; JEOL, Tokyo, Japan), operated at 200 kV. The entrance aperture of the spectrometer was 5 mm, and a camera length of 20 mm was used, resulting in a collection semi-angle of 83 mrad. To acquire spectra, a dispersion of 0.25 eV/channel was used, leading to a FWHM of 0.75 eV of the zero-loss peak. The local elemental distribution with nano-scale spatial resolution within the crystalline grains was analyzed by an energy-dispersive x-ray spectrometer (Centurio, JEOL) in STEM mode. The thin lamella for the analyses was prepared by Focused Ion Beam milling (FIB) on an SEM platform, (JIB 4601 F Multi-Beam, JEOL Ltd.) with a 30 kV ion energy. Ion milling with different ion beam currents (from 10 nA, down to 100 pA) was applied until an electron-transparent foil of ca. 100 nm-thickness was obtained. For the in-situ lift-out step, the thinned lamella was mounted to a supporting half copper grid by using a micromanipulator.

3. Results and discussion

3.1 Microstructure

Residual pores are the main source of light scattering that limit transparency in ceramics. The size and total volume of these residual pores are controlled by the pore characteristics (i.e., fraction, size, and distribution) of green bodies. Complete densification in subsequent sintering process is expected when green bodies benefit from high density, small pore size, and narrow pore size distribution [25]. Indeed, uniform particle coordination impedes locally different shrinkages and restricts pore coarsening during consolidation [26]. Colloidal processing generally allows the reduction of size and number of pores in green bodies by providing particles freedom to arrange themselves in packing-efficient configurations [22], [27]. Nevertheless, fine nanoparticles (e.g., <15 nm) tend to form agglomerates, owing to their high surface area (e.g., SBET of 3YSZ nanoparticle as 117 m^2/g in this work) and reactivity [28]. Consequently, the formation of uniform green bodies without coarse heterogeneities demands effective powder processing and shaping methods.

Green bodies that were formed at pressures lower than 10 bar required higher sintering temperatures (e.g., >1250 °C) for full densification and as a result, the final grain size was beyond 100 nm (e.g., 110–180 nm, Fig. S3). On the other hand, green bodies filtered at pressures > 40 bar (T.D. >52%) were more prone to cracking during drying, debinding, or sintering (Fig. S4). Among green bodies tested and irrespective of yttria content, samples that were filtered at 20 bar (showing 52% > T.D. > 50%) were fully densified (>99.5% T.D.) at temperature of 1100–1200 °C (T.D. of 1.5 YSZ as 6.15 g/cm3, 3YSZ as 6.09 g/cm3, and 8YSZ as 5.95 cm3). Thus, 50.5 ± 0.5 T.D. was considered as the criteria to use the green samples throughout the rest of the work. Fig. 1a represents the pore size evolution of 3YSZ filtered samples as a function of thermal-treatment temperature. The Barrett-Joyner-Halenda (BJH) profile demonstrates a nearly symmetrical distribution of interconnected pores with average diameter of 4.2 nm in green bodies. As temperature increases during sintering, uniform growth is noticeable and the average pore diameter reaches 8.7 nm at 800 °C. This uniform change in pore size is also manifested by a single narrow peak of shrinkage rate in the dilatometry curve (Fig. 1b) implying the presence of a narrow pore size distribution with no agglomerate across the sample [29]. It is worth noting that the two peaks at temperature < 400 °C are related to dehydroxylation of nanoparticles and organic burn-out (Fig. S5 and Table S1).

Increasing temperature beyond 900 °C breaks the interconnected porosity network and forms individual pores (Fig. S6). As a result, pore analysis by N_2 sorption is no longer applicable. In order to assess the size of residual pores as well as size of grains after sintering, the samples were characterized by SEM (Fig. S7). Typical microstructures of 3YSZ and 8 YSZ ceramics are shown in Fig. 2, confirming the high degree of densification with average grains size of 75 nm and 85 nm, respectively. In both cases, residual pores with a maximum diameter of < 15 nm could be detected at the triple points of some grains (Fig. 2c). These results support the miniaturization of residual pores to diameters of < 15 nm and grains of < 85 nm, which was found also valid in all zirconia ceramics obtained with sintering temperatures ranging from 1150 °C to 1200 °C.

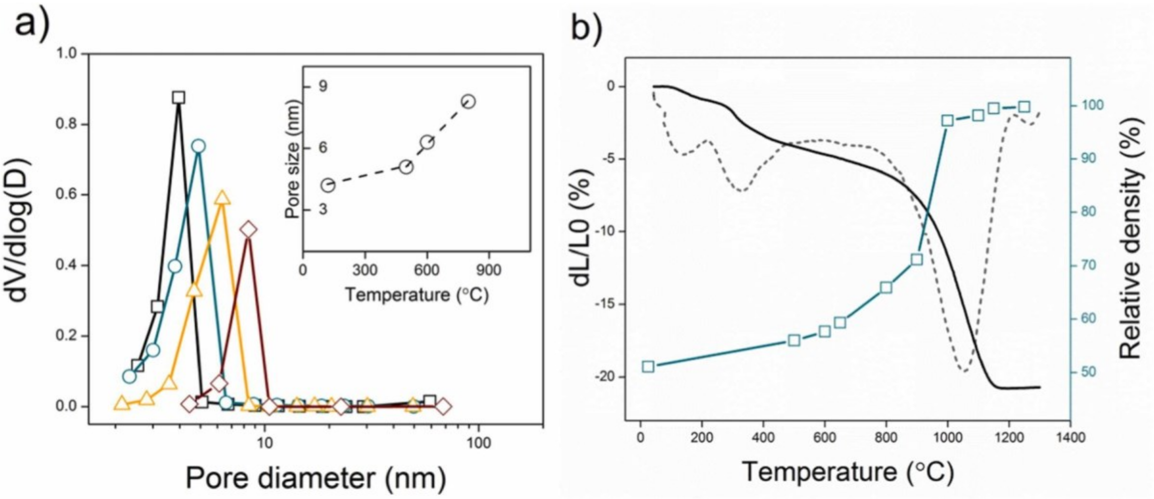

Figure 1: a) Pore size distribution as a function of temperature of densification; 120 °C (☐), 500 °C (○), 600 °C (Δ), and 800 °C (◇) and b) effect of temperature on the linear shrinkage and relative density (dash line shows the shrinkage rate) of samples with a green density 50.5 ± 0.5 T.D. All samples here are formed from 3YSZ with primary particle size of 8 nm. Inset in (a) shows the average pore size of samples as a function of temperature.

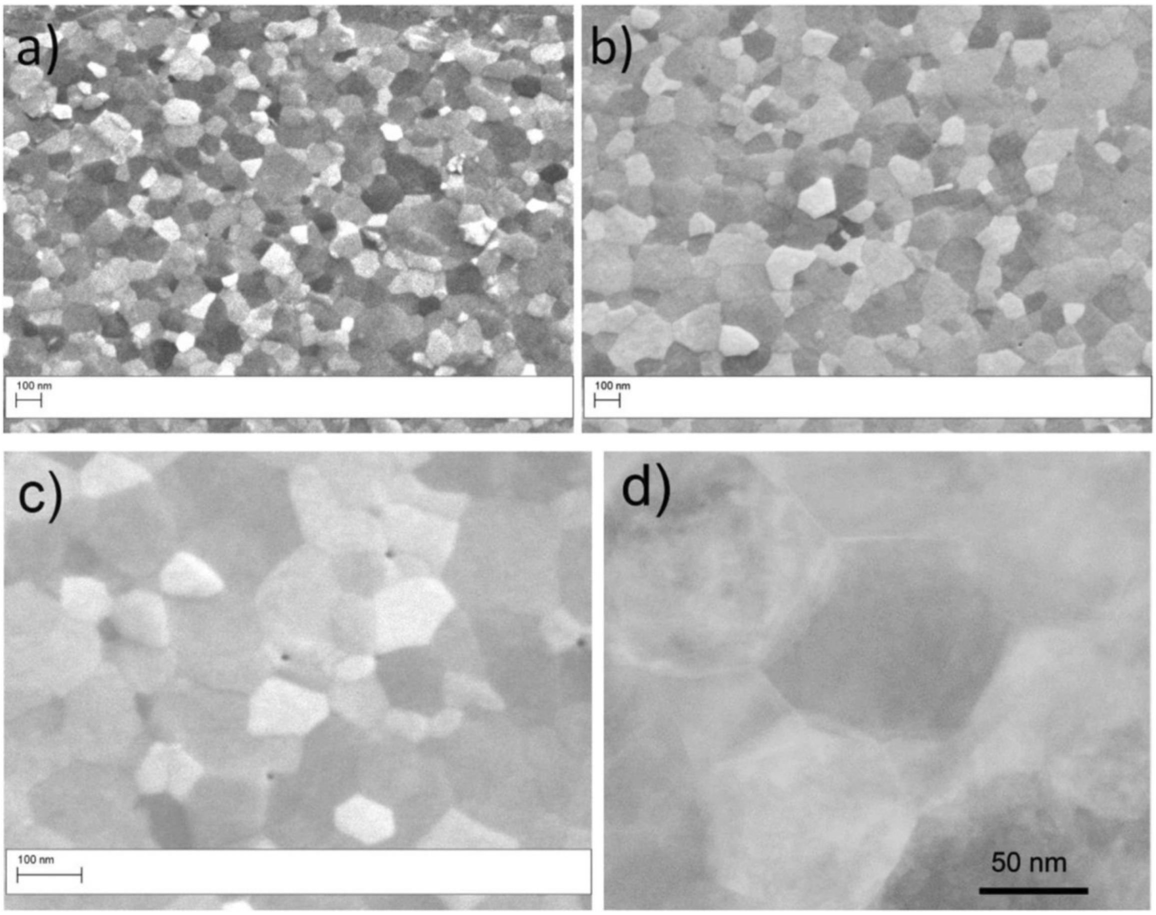

Figure 2: SEM image of fully dense a) 3YSZ and b) 8YSZ sintered at 1150 °C and 1200 °C, respectively. Representative SEM (c) and high-angle annular dark-field image in STEM (d) of 3YSZ at higher magnification showing the nanoscale range of residual pores (size of <15 nm) and fully densified structure, respectively. The nanopores in (c) are not prevalent as the density of the samples is 6.06 ± 0.01 g/cm^3.

3.2 Optical properties

In the visible domain and when birefringence is significant, apart from residual pores, grain boundaries are the main source of light scattering in non-cubic ceramics. Scattering by grain boundaries (GBs) depends on the grain size (= GBs density) in relation with the wavelength used (for infrared light, grains with a size of about 500 nm will be invisible). Furthermore, a non-cubic ceramic like alumina with very low birefringence (about 0.007) will be less sensitive to light scattering. The Rayleigh approximation [4] can be used as a straight-forward model to estimate the real in-line transmission (i.e, RIT, as a measure of transparency) of a high purity, dense (no pore), and non-cubic ceramic in which RIT is inversely proportional to the average birefringence and grain size at a fixed thickness (Eq. 1).

$$T_{In-line} = (1-R)exp\left\{-\left(\frac{128\pi^4 r^3}{18\lambda^4}\right)\left[\frac{\Delta n_{ave}(2n+\Delta n_{ave})}{2}\right]^2 t\right\} \qquad \text{Eq. 1}$$

Δn_{ave} is the average birefringence, 2r is the grain size, t is the thickness, n is the refractive index (e.g., 2.19 and 2.15 for 3YSZ and 8YSZ, respectively at λ of 633 nm), λ is the wavelength of the incident light, and $R= 1–2\ n/(n_2 +1)$ is the reflection loss at two surfaces of a sample. In our case, the band gap of YSZ is high enough for considering no absorption in Eq. 1. Taking into account the criterion for Rayleigh scattering ($2\pi rn/\lambda < 1$), the model is valid for grain size of 50–110 nm in 3YSZ ceramics [6], [10], and is consistent with the grain size of our specimens. From Klimke et al. [4], given the birefringence of 0.03–0.04 in 3YSZ, an RIT greater than 20% in the visible range necessitates a grain size of < 80 nm in a sample of 1 mm thickness in the direction of the optical path. On the other hand, when Δn_{ave}= 0 (cubic zirconia, e.g., 8YSZ), the RIT becomes independent of grain size and loss of transmitted light is only attributed to the reflection at the surfaces. In the absence of other source of light scattering such as impurities, pore, secondary phases, and coloring centers, the maximum RIT of a dense YSZ ceramic can be estimated as ~76% of the incident light for entire visible spectrum [4].

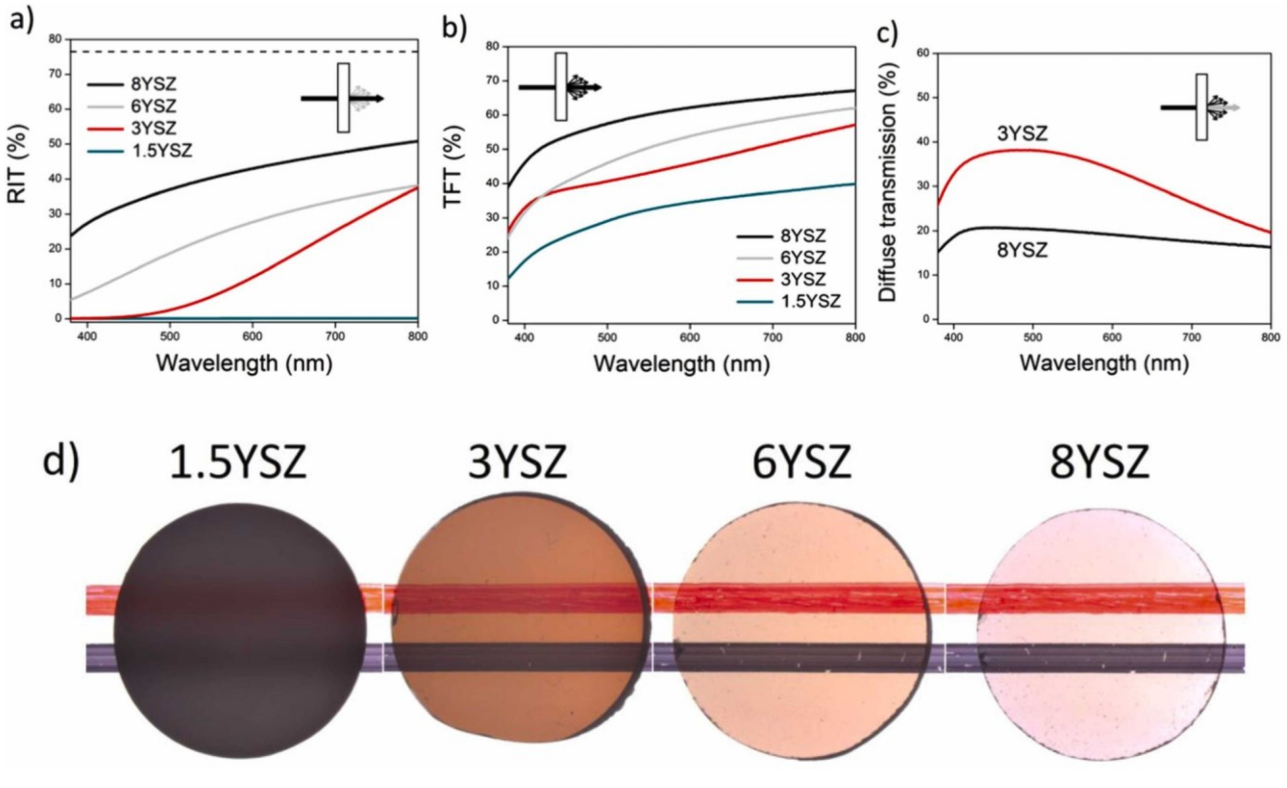

Figure 3: Optical spectra of 1 mm-thick polished samples with grain size of 75 ± 5 nm; a) RIT, b) TFT, and c) diffuse transmission, and d) appearance of discs with diameter of 12.0 ± 0.5 mm and thickness of 1.00 ± 0.02 mm under transmitted light. Images were captured under same illumination and background conditions. The dashed line in (a) shows the maximum theoretical RIT of a dense YSZ ceramic estimated as ~76%. The 1.5YSZ and 6YSZ samples are reported for comparison.

Based on the size of residual nano-pores, nano-grained microstructure, and high purity of our samples—no coloring centers and impurities (Table S2), we anticipated a high degree of translucency/transparency in our samples. Fig. 3 confirms this hypothesis by showing the optical spectra as well as appearance of 1-mm thick specimens with average grain size of 75 ± 5 nm. The 8YSZ presents a maximum in-line transmittance of 51% at 800 nm with gradual decrease to 25% at λ = 380 nm. In a similar way, the transmission of 3YSZ is above 10% for λ > 580 nm with a maximum of 38% at 800 nm wavelength. Interestingly, the light transmission of 8YSZ and 3YSZ here is higher than the reported values for samples manufactured by HIP-SPS with even smaller grain size (e.g., 50 nm) [4], [13], [18], [30].

To gain insight into the high RIT of YSZ samples, we first characterized them by Total Forward Transmission (TFT) and then, calculated the diffuse transmission ($T_{diffuse}$=TTFT – TRIT). As shown in Fig. 3b, both TFT and RIT increase with λ and yttria content. TFT increase partly correlates with the decreasing refractive indices as a function of the wavelength of the incident light. [6] RIT increase is directly linked to the content of cubic phase which inherently promotes transparency (Fig. S8 and Table S3). A significant difference between TFT and RIT can be noticed in tetragonal zirconia, especially in the shorter wavelength range. By contrast, cubic zirconia shows a similar trend for in-line and total forward transmission and the diffuse transmission is less sensitive to the wavelength compared to that of 3YSZ (Fig. 3c). Considering the absence of birefringence in cubic zirconia, this wavelength independence suggests that the loss of RIT in 8YSZ stems from residual nano-pores. Although scattering efficiency of pores markedly decreases in the nano-range, total pore volume still plays a key role in diffuse transmission. Numerical studies reveal further details about the correlation between RIT and pore size-volume. For RIT loss below 20% in cubic zirconia with pore size of 10–15 nm, the relative density of 99.7% is required (V_{pore}< 3000 ppm) [9], [31]. This result is in agreement with density of our samples (5.94 ± 0.01 g/cm^3) and supports the fact that the high RIT of 8YSZ in the entire spectrum originates from miniaturization and elimination of residual pores.

In the case of tetragonal zirconia, grain boundaries also scatter light and both residual porosity and size determine the extent of diffuse scattering. Ultra-fine grains with a size of < 30 nm would be practically invisible to the incident visible light. As grain size increases, the interaction between grains and light intensifies. Light with shorter wavelengths can be effectively scattered in 3YSZ with an average size of 75 nm [10], whereas scattering becomes less pronounced at longer wavelengths owing to the direct correlation between RIT and λ (Eq. 1). Therefore, as opposed to nano-pores, the dependency of $T_{diffuse}$ and λ in this range of grain size makes the diffuse transmission behavior elliptic (as a function λ) and promotes the loss of RIT in 3YSZ (Fig. 3c). The effect of scattering centers on RIT was further explored by synthesis of a fully dense 3YSZ (99.9% of T.D.) with an average grain size of 50 nm (Fig. S9), densified by HIP (referred to HIP50). The light transmission of HIP50 after annealing in air (Fig. S10) is consistent with that of reported by Anselmi-Tamburini et al. [18] However, surprisingly, both RIT and TFT of 3YSZ with grain size of 75 nm (pressure-less sintered) are still higher than those of HIP50. The development of high concentrations of point defects, in the form of oxygen vacancies, was suggested as the origin of significant light absorption in the latter [18]. To test this conjecture, we investigated the local environment (e.g. oxygen coordination) of Zr cations by analyzing the Energy Loss Near Edge Structure (ELNES) fingerprints of the characteristic Zr-M ionization edges in nano-grains of 3YSZ and HIP50 specimens. This is possible as subtle changes in the number and spatial arrangements of the atoms in the first nearest neighbor shell around the ionized atom in electron energy loss spectroscopy (EELS) result in characteristic differences in the shape of ELNES features [32].

Fig. 4 shows a comparison between representative EELS spectra after background subtraction by a power-law model and removal of multiple scattering by Fourier-ratio deconvolution. The EELS spectrum of the stoichiometric ZrO2 standard sample (JEOL, Tokyo, Japan) is also presented as the reference spectrum for comparison. The ionization peaks in the range of 180–250 eV, 340–360 eV, and 540–550 eV are associated with the Zr-$M_{2,3}$, Zr-$M_{4,5}$, and O-K ionization edges, respectively [33]. The identical ELNES features of the Zr-M and O-K edges in samples are indicative of a similar local environment and bonding of zirconium to the oxygen. We did not notice significant differences in local oxygen coordination of Zr^{4+} cations in other point analyses that could be correlated with the reducing atmosphere of HIP. This shows the efficiency of an annealing in air to recover oxygen stoichiometry. On the other hand, a pronounced C-K edge at 280 eV was observed in the EELS spectrum of HIP50. Carbon centers (C-centers) were also detected by energy dispersive X-ray spectroscopy (EDS) with evidence of accumulation in grain boundaries (~1.8 at%, Table S4, Fig. S11). These observations indicate that optical properties of HIP50 are controlled by the presence of C-centers in significant amounts and not by oxygen vacancies. Therefore, the high RIT of 3YSZ in this work is directly attributed to the reduced size of grains and residual pores while avoiding the formation of other sources of light absorption such as C-centers and impurities that are difficult to avoid or suppress with HIP or other pressure-assisted methods such as SPS with graphite dies.

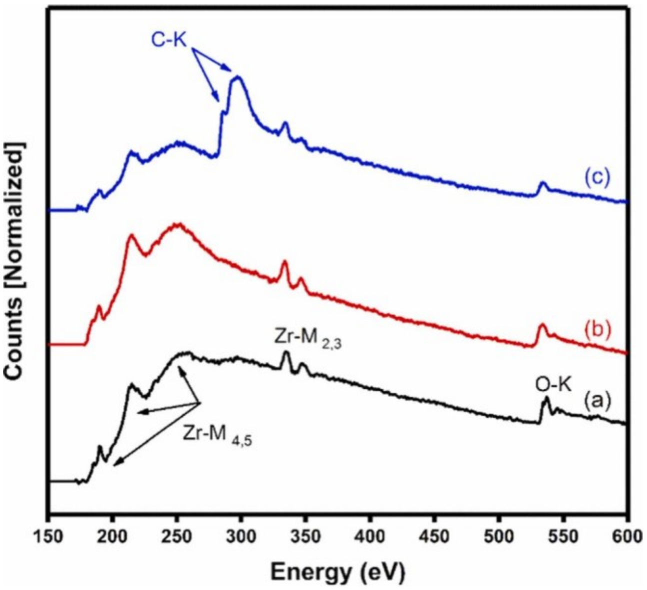

Figure 4: EELS spectra of a) stoichiometric ZrO_2, b) nano-grain 3YSZ, and c) HIP50 after annealing in air.

3.3 Mechanical properties

The strong chemical bonds and the consequent limited dislocation mobility govern the strong resistance to plastic deformation in ceramics. Like in metals, grain boundaries (GBs) act as additional obstacles for movement of dislocations, resulting in an exceptionally high stress needed for plasticity in polycrystalline ceramics. The effect of grain size on yield strength and hardness, often referred to as Hall-Petch relation, is described by the linear dependence between the hardness (or yield strength) and the inverse square root of grain size [34], [35], [36], [37]. In addition to dislocation motion, tetragonal zirconia ceramics may exhibit transformation-induced plasticity under stress field [38]. This sudden rearrangement from meta-stable tetragonal to stable monoclinic phase (t→m transformation) is accompanied by ~4% volumetric expansion and also by twinning and formation of shear bands in the structure. The latter can be microscopically observed as surface corrugations [39], [40], [41]. The stability of tetragonal phase is dependent on doping content and grain size. The lower yttria content and larger grain size, favoring the t→m transformation [22], [42], determine the extent of plastic deformation and, thus, mechanical properties of tetragonal zirconia ceramics.

The biaxial strength (σ_f), hardness (H_v) and indentation fracture toughness (K_{IC}) of zirconia samples with grain size of 75 ± 5 nm are plotted as a function of composition in Fig. 5. The cubic zirconia (8YSZ) shows strength of 680 ± 60 MPa, hardness of 14.3 ± 0.2 GPa, and K_{IC} of 1.5 $MPa\cdot m^{1/2}$. Biaxial strength of YSZ gradually improves by decreasing yttria content, in the region 8–3.5 mol.%. Below this value, a significant increase to ~2 GPa is first showed for 3YSZ, followed by a further rise with lower yttria contents, finally reaching a value as high as ~2.6 GPa for 1.5YSZ. The abrupt increase in biaxial strength at ~3 mol. % yttria coincides with a slight drop in hardness from 14.2 ± 0.2 to 13.2 ± 0.2 GPa. Variation in K_{IC} as a function of yttria content is also similar to that of biaxial strength. However, the sudden change occurs at lower yttria content (from 2YSZ to 1.5YSZ) and it is concurrent to the second decrease in hardness from 13.0 ± 0.2 to 12.2 ± 0.1.

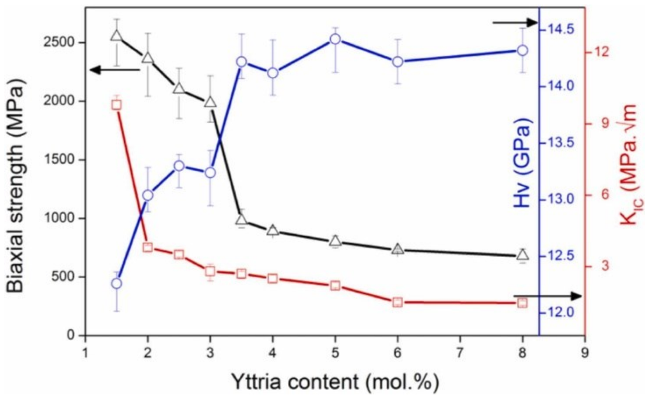

Figure 5: Biaxial strength (Δ), hardness (◯), and, indentation fracture toughness (☐) of YSZ with grain size 75 ± 5 nm as a function of yttria content.

The analysis of vicinity of indentation cracks is useful to gain deeper understanding about the mechanism behind these observations. Fig. 6a and b show the tip of indentation cracks in 8YSZ samples with average grain size of 160 nm and 80 nm, respectively. The former was produced from same green bodies but specifically heat treated at 1250 °C for 3 h to obtain submicron grain size.

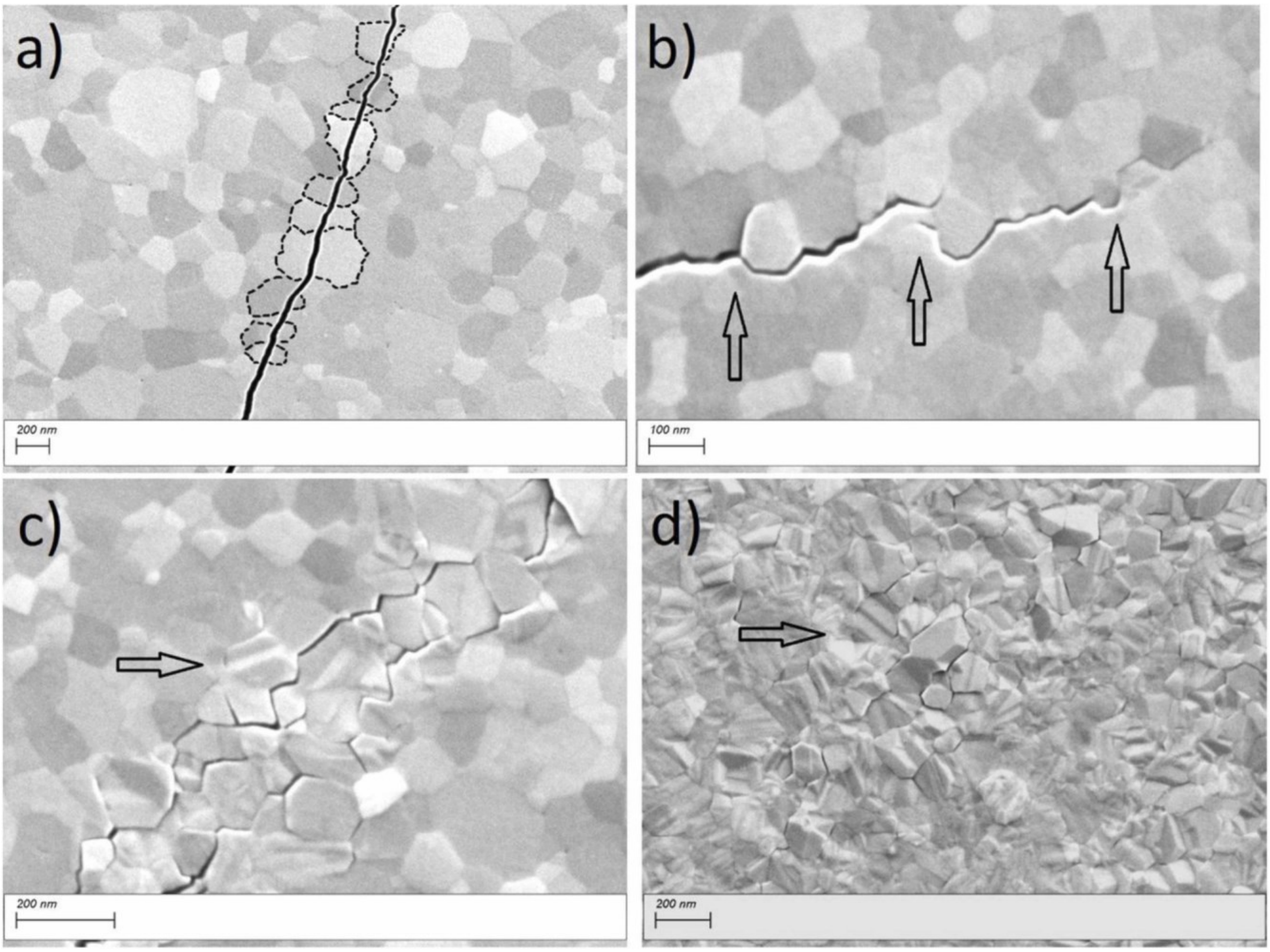

Figure 6: Vicinity of indentation cracks in a) 8YSZ with grain size of 160 nm and b) 8YSZ with grain size of 80 nm, c) 3YSZ with grain size of 80 nm, and d) 1.5YSZ with grain size of80 nm. Dash-lines are added to (a) to highlight GBs. Arrows in (b) show bridging, wedging, and deflection of the crack from left to right. Arrows in (c) and (d) show exemplary twinning and surface corrugations resulted from t→m transformation.

Fracture path shifts from mostly transgranular in the 'large grain' (d_{grains}=160 nm) samples to mostly intergranular in fine grain (d_{grains}=80 nm) microstructures showing deflection, bridging, and wedging of cracks. Comparing the σ_f and H_v values with micron grain-sized 8YSZ [9], [28] (bending strength of 250–400 MPa and hardness of 11.8–12.3 GPa in samples with grain size of 17–70 µm), the effect of nano-grained structure on improving strength and hardness of zirconia ceramics correlates with the small defect size and impeding effect of GBs on dislocation movement [1], [43]. Biaxial strength of zirconia samples increases with decreasing yttria content (from 8 mol. % to 3.5 mol. %) in the structure. This change is consistent with the experimental and molecular dynamics simulations of single crystal YSZ, demonstrating that higher the yttria content, higher the local weak points which facilitate the dislocation motion [44], [45]. On the other hand, direct relation between hardness and yttria composition is attributed to the variation in content of cubic phase (Table S3) which is inherently a harder phase owing to the stabilizing effect yttria as well as non-transformability of tetragonal phase with yttria > 4 mol. % [46]. Once the structure is fully transformable (tetragonal, 3YSZ Table S3), martensitic phase transformation becomes active (Fig. 6c). Activation of the t→m transformation as the second plastic deformation mechanism decreases the hardness of YSZ. On the other hand, it can synergize with nano-grained structure by reducing the stress-intensity at the crack tip [47] and interfere with crack propagation (Fig. S12 and [12], [48]) and consequently, alludes to the high strength of tetragonal zirconia.

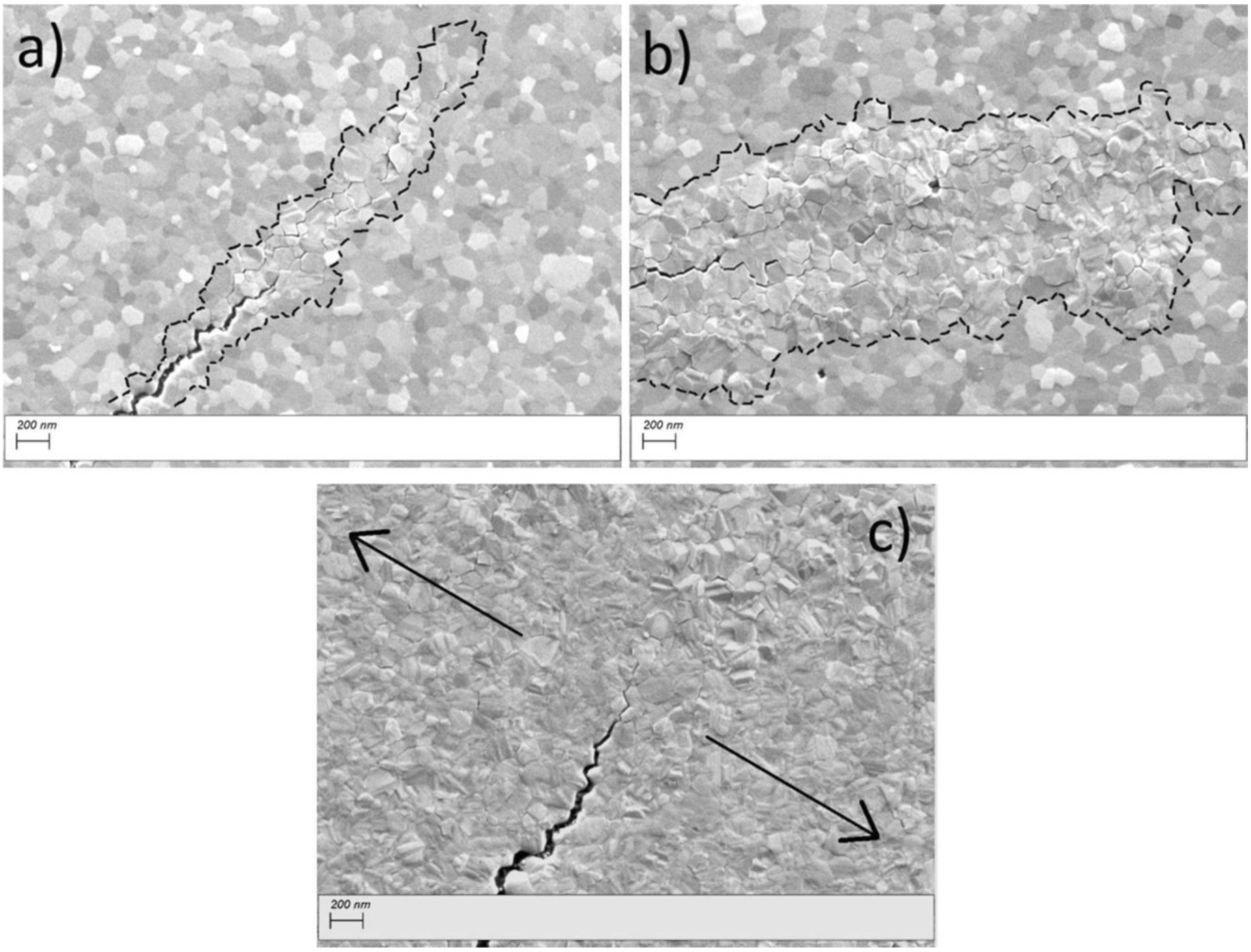

Figure 7: Vicinity of indentation cracks in tetragonal YSZ with grain size of 75 ± 5 nm; a) 3YSZ, b) 2YSZ, and c) 1.5YSZ. Dash-lines in (a) and (b) highlight the boundary of transformed zone around the crack. Arrows in (c) shows the width of transformed zone around the crack.

Decreasing the yttria content to 1.5 mol. % changes the dominant mechanism of energy dissipation from intergranular cracking to transgranular phase transformation (Fig. 6d) and further improves the strength of YSZ. Dominancy of t→m transformation mechanism is also manifested by observing the second drop in hardness and significant growth in KIC. Fig. 7 shows the vicinity of indentation cracks in tetragonal YSZ at lower magnification. The t→m transformation in 3YSZ is limited to few grains in front of the crack (Fig. 7a) and deflection/bridging during intergranular fracture (Fig. 6c) is still active as crack-tip shielding mechanism [43]. As the yttria content decreases, the transform-zone around the crack-tip increases (Fig. 7b) and the t→m transformation becomes the primary source of toughening in 1.5 YSZ (Fig. 7c and Fig. S13). Therefore, the pronounced strength and hardness of tetragonal YSZ compared to micron grain-sized samples is directly linked to the grain refinement and activation of stress-induced phase transformation, even in this range of grain sizes.

4. Summary and conclusion

We report on the preparation of nano-grain YSZ ceramics with density > 99.5% T.D. through conventional pressure-less sintering. Green body density > 50% T.D., narrow pore size distribution centered at ~4 nm, and use of highly reactive nanoparticles with primary particle size of < 10 nm are crucial to reduce the densification temperature to 1100–1200 °C (with dwell time of 1–2 h) and thus, obtain nano-crystalline structures. Decreasing the grain size to < 85 nm significantly improves light transmission and biaxial strength of YSZ compared to both nano-crystalline zirconia ceramics synthesized by high pressure sintering techniques such as HIP/SPS and micron/sub-micron grain-size zirconia counterparts (Table S5). The pronounced light transmission of 3YSZ and 8YSZ in this work is directly related to the nano-grains and both miniaturization and elimination of residual pores while avoiding formation of other source of light scattering such as carbon contaminations and impurities. High strength and hardness correlate with microstructure refinement in cubic zirconia and activation of both intergranular deformation and martensitic phase transformation which is still active even in nano-sized tetragonal zirconia. These results will potentially open up venues for preparation of transparent ceramics while keeping high strength through simple, scalable, and producible route.

Funding:

The authors declare no competing financial interest

Declaration of Competing Interest

The authors declare that they have no known competing financial interests or personal relationships that could have appeared to influence the work reported in this paper.

References

1. K. Serivalsatit, B. Kokuoz, B. Yazgan-Kokuoz, M. Kennedy, J. Ballato, Synthesis, processing, and properties of submicrometer-grained highly transparent yttria ceramics, J. Am. Ceram. Soc., 93 (5) (2010), pp. 1320-1325
2. M.R. du Merac, M. Bram, J. Malzbender, M. Ziegner, M. Rasinski, O. Guillon, Increasing fracture toughness and transmittance of transparent ceramics using functional low-thermal expansion coatings, Sci. Rep., 8 (1) (2018), p. 15644
3. A. Goldstein, A. Krell, Transparent ceramics at 50: progress made and further prospects, J. Am. Ceram. Soc., 99 (10) (2016), pp. 3173-3197
4. J. Klimke, M. Trunec, A. Krell, Transparent tetragonal yttria-stabilized zirconia ceramics: influence of scattering caused by birefringence, J. Am. Ceram. Soc., 94 (6) (2011), pp. 1850-1858
5. W. Pabst, S. Hříbalová, Light scattering models for describing the transmittance of transparent and translucent alumina and zirconia ceramics, J. Eur. Ceram. Soc., 41 (3) (2021), pp. 2058-2075
6. A. Krell, J. Klimke, T. Hutzler, Transparent compact ceramics: inherent physical issues, Opt. Mater., 31 (8) (2009), pp. 1144-1150
7. I. Yamashita, H. Nagayama, K. Tsukuma, Transmission properties of translucent polycrystalline alumina, J. Am. Ceram. Soc., 91 (8) (2008), pp. 2611-2616
8. H.B. Zhang, B.N. Kim, K. Morita, H. Yoshida, J.H. Lim, K. Hiraga, Optimization of high-pressure sintering of transparent zirconia with nano-sized grains, J. Alloy. Compd., 508 (1) (2010), pp. 196-199

9. I. Yamashita, K. Tsukuma, Light scattering by residual pores in transparent zirconia ceramics, J. Ceram. Soc. Jpn., 119 (1386) (2011), pp. 133-135
10. Y. Zhang, Making yttria-stabilized tetragonal zirconia translucent, Dent. Mater., 30 (10) (2014), pp. 1195-1203
11. Y. Xiong, J. Hu, Z. Shen, Dynamic pore coalescence in nanoceramic consolidated by two-step sintering procedure, J. Eur. Ceram. Soc., 33 (11) (2013), pp. 2087-2092
12. M.A. Meyers, A. Mishra, D.J. Benson, Mechanical properties of nanocrystalline materials, Prog. Mater. Sci., 51 (4) (2006), pp. 427-556
13. R. Lach, M.M. Bućko, K. Haberko, M. Sitarz, K. Cholewa-Kowalska, From nanometric zirconia powder to transparent polycrystal, J. Eur. Ceram. Soc., 34 (16) (2014), pp. 4321-4326
14. J.E. Alaniz, F.G. Perez-Gutierrez, G. Aguilar, J.E. Garay, Optical properties of transparent nanocrystalline yttria stabilized zirconia, Opt. Mater., 32 (1) (2009), pp. 62-68
15. K. Lu, Sintering of nanoceramics, Int. Mater. Rev., 53 (1) (2008), pp. 21-38
16. F. Maglia, I.G. Tredici, U. Anselmi-Tamburini, Densification and properties of bulk nanocrystalline functional ceramics with grain size below 50nm, J. Eur. Ceram. Soc., 33 (6) (2013), pp. 1045-1066
17. H. Zhang, B.-N. Kim, K. Morita, H. Yoshida, J.-H. Lim, K. Hiraga, Optical properties and microstructure of nanocrystalline cubic zirconia prepared by high-pressure spark plasma sintering, J. Am. Ceram. Soc., 94 (9) (2011), pp. 2981-2986
18. U. Anselmi-Tamburini, J.N. Woolman, Z.A. Munir, Transparent nanometric cubic and tetragonal zirconia obtained by high-pressure pulsed electric current sintering, Adv. Funct. Mater., 17 (16) (2007), pp. 3267-3273
19. J.W. Drazin, J.A. Wollmershauser, H. Ryou, M.A. Wolak, E.P. Gorzkowski, Pressureless low temperature sintering of nanocrystalline zirconia ceramics via dry powder processing, J. Am. Ceram. Soc., 103 (1) (2020), pp. 60-69
20. A. Krell, T. Hutzler, J. Klimke, A. Potthoff, Fine-grained transparent spinel windows by the processing of different nanopowders, J. Am. Ceram. Soc., 93 (9) (2010), pp. 2656-2666
21. M. Mazaheri, A. Simchi, F. Golestani-Fard, Densification and grain growth of nanocrystalline 3Y-TZP during two-step sintering, J. Eur. Ceram. Soc., 28 (15) (2008), pp. 2933-2939
22. J. Binner, B. Vaidhyanathan, Processing of bulk nanostructured ceramics, J. Eur. Ceram. Soc., 28 (7) (2008), pp. 1329-1339
23. C.J. Szepesi, J. Cantonnet, R.A. Kimel, J.H. Adair, A critical assessment of nanometer-scale zirconia green body formation by pressure filtration and uniaxial compaction, J. Am. Ceram. Soc., 94 (12) (2011), pp. 4200-4206
24. G.R. Anstis, P. Chantikul, B.R. Lawn, D.B. Marshall, A critical evaluation of indentation techniques for measuring fracture toughness: I, direct crack measurements, J. Am. Ceram. Soc., 64 (9) (1981), pp. 533-538
25. M. Mazaheri, Z.R. Hesabi, F. Golestani-Fard, S. Mollazadeh, S. Jafari, S.K. Sadrnezhaad, The effect of conformation method and sintering technique on the densification and grain growth of nanocrystalline 8 mol% yttria-stabilized zirconia, J. Am. Ceram. Soc., 92 (5) (2009), pp. 990-995
26. M. Yoshida, S. Takeno, O. Sakurada, Fabrication of translucent tetragonal zirconia by gelcasting of thin zirconia nano-slurry, J. Ceram. Soc. Jpn., 124 (5) (2016), pp. 500-505
27. I. Santacruz, K. Anapoorani, J. Binner, Preparation of high solids content nanozirconia suspensions, J. Am. Ceram. Soc., 91 (2) (2008), pp. 398-405
28. D. Hotza, D.E. García, R.H.R. Castro, Obtaining highly dense YSZ nanoceramics by pressureless, unassisted sintering, Int. Mater. Rev., 60 (7) (2015), pp. 353-375
29. P. Durán, P. Recio, J.R. Jurado, C. Pascual, C. Moure, Preparation, sintering, and properties of translucent Er2O3-doped tetragonal zirconia, J. Am. Ceram. Soc., 72 (11) (1989), pp. 2088-2093

30. A. Dash, B.-N. Kim, J. Klimke, J. Vleugels, Transparent tetragonal-cubic zirconia composite ceramics densified by spark plasma sintering and hot isostatic pressing, J. Eur. Ceram. Soc., 39 (4) (2019), pp. 1428-1435
31. S.F. Wang, J. Zhang, D.W. Luo, F. Gu, D.Y. Tang, Z.L. Dong, G.E.B. Tan, W.X. Que, T.S. Zhang, S. Li, L.B. Kong, Transparent ceramics: processing, materials and applications, Prog. Solid State Chem., 41 (1) (2013), pp. 20-54
32. V.J. Keast, A.J. Scott, R. Brydson, D.B. Williams, J. Bruley, Electron energy-loss near-edge structure – a tool for the investigation of electronic structure on the nanometre scale, J. Microsc., 203 (2) (2001), pp. 135-175
33. N. Ni, S. Lozano-Perez, J. Sykes, C. Grovenor, Quantitative EELS analysis of zirconium alloy metal/oxide interfaces, Ultramicroscopy, 111 (2) (2011), pp. 123-130
34. A. Bokov, J.B. Rodrigues Neto, F. Lin, R.H.R. Castro, Size-induced grain boundary energy increase may cause softening of nanocrystalline yttria-stabilized zirconia, J. Am. Ceram. Soc., 103 (3) (2020), pp. 2001-2011
35. D.N.F. Muche, J.W. Drazin, J. Mardinly, S. Dey, R.H.R. Castro, Colossal grain boundary strengthening in ultrafine nanocrystalline oxides, Mater. Lett., 186 (2017), pp. 298-300
36. J.A. Wollmershauser, B.N. Feigelson, E.P. Gorzkowski, C.T. Ellis, R. Goswami, S.B. Qadri, J.G. Tischler, F.J. Kub, R.K. Everett, An extended hardness limit in bulk nanoceramics, Acta Mater., 69 (2014), pp. 9-16
37. C. Yang, A. Thron, R.H.R. Castro, Grain boundary strengthening in nanocrystalline zinc aluminate, J. Am. Ceram. Soc., 102 (11) (2019), pp. 6904-6912
38. R.C. Garvie, R.H. Hannink, R.T. Pascoe, Ceramic steel?, Nature, 258 (5537) (1975), pp. 703-704
39. N. Zhang, M. Asle Zaeem, Understanding specimen- and grain-size effects on nanoscale plastic deformation mechanisms and mechanical properties of polycrystalline yttria-stabilized tetragonal zirconia nanopillars, Eur. J. Mech. A/Solids, 76 (2019), pp. 80-90
40. F.F. Lange, Transformation toughening, J. Mater. Sci., 17 (1) (1982), pp. 225-234
41. X.M. Zeng, A. Lai, C.L. Gan, C.A. Schuh, Crystal orientation dependence of the stress-induced martensitic transformation in zirconia-based shape memory ceramics, Acta Mater., 116 (2016), pp. 124-135
42. A. Bravo-Leon, Y. Morikawa, M. Kawahara, M.J. Mayo, Fracture toughness of nanocrystalline tetragonal zirconia with low yttria content, Acta Mater., 50 (18) (2002), pp. 4555-4562
43. M.E. Launey, R.O. Ritchie, On the fracture toughness of advanced materials, Adv. Mater., 21 (20) (2009), pp. 2103-2110
44. N. Zhang, M.A. Zaeem, Effects of specimen size and yttria concentration on mechanical properties of single crystalline yttria-stabilized tetragonal zirconia nanopillars, J. Appl. Phys., 122 (1) (2017), Article 014302
45. K. Otsuka, A. Kuwabara, A. Nakamura, T. Yamamoto, K. Matsunaga, Y. Ikuhara, Dislocation-enhanced ionic conductivity of yttria-stabilized zirconia, Appl. Phys. Lett., 82 (6) (2003), pp. 877-879
46. G.P. Cousland, X.Y. Cui, A.E. Smith, A.P.J. Stampfl, C.M. Stampfl, Mechanical properties of zirconia, doped and undoped yttria-stabilized cubic zirconia from first-principles, J. Phys. Chem. Solids, 122 (2018), pp. 51-71
47. R.M. McMeeking, A.G. Evans, Mechanics of transformation-toughening in brittle materials, J. Am. Ceram. Soc., 65 (5) (1982), pp. 242-246
48. N. Zhang, M. Asle Zaeem, Competing mechanisms between dislocation and phase transformation in plastic deformation of single crystalline yttria-stabilized tetragonal zirconia nanopillars, Acta Mater., 120 (2016), pp. 337-347

Appendix A. Supplementary materials

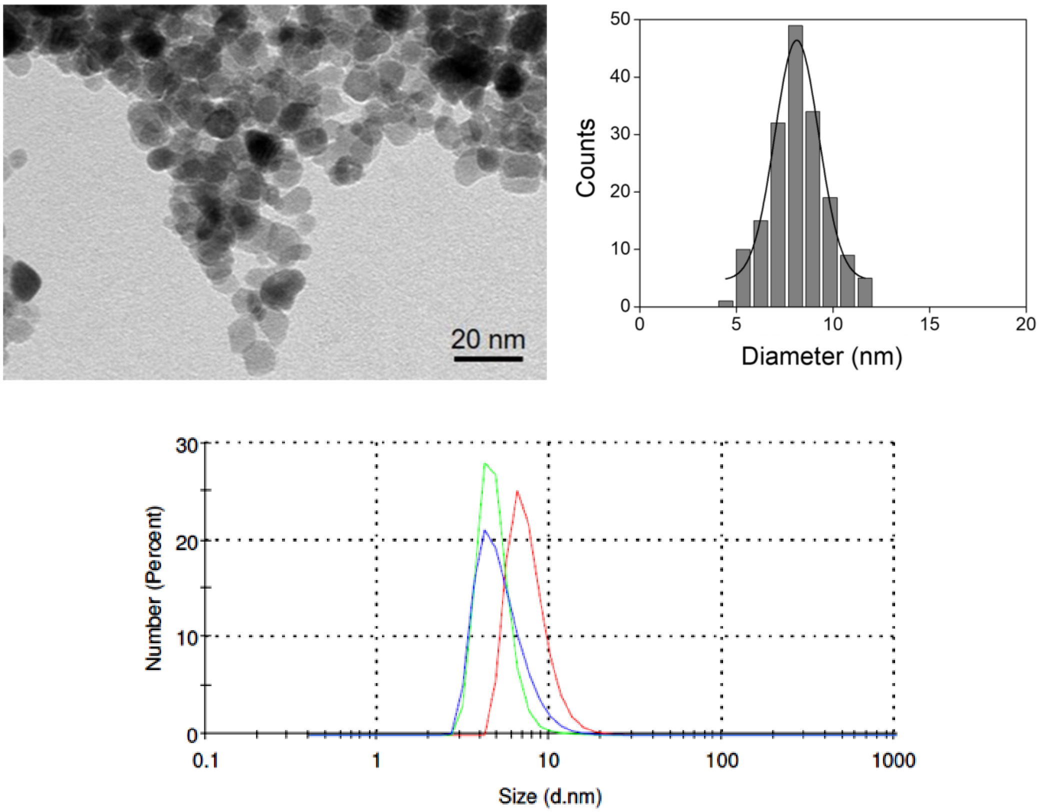

Figure S1.TEM and particle size distribution measured from TEM images (top) and dynamic light scattering of suspensions after synthesis (bottom) showing nanoparticles with an average size of 8 ± 1 nm

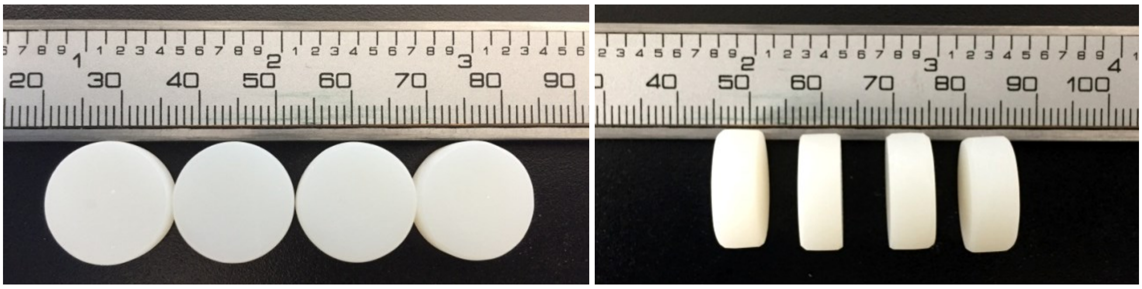

Figure S2. Dried samples after grinding

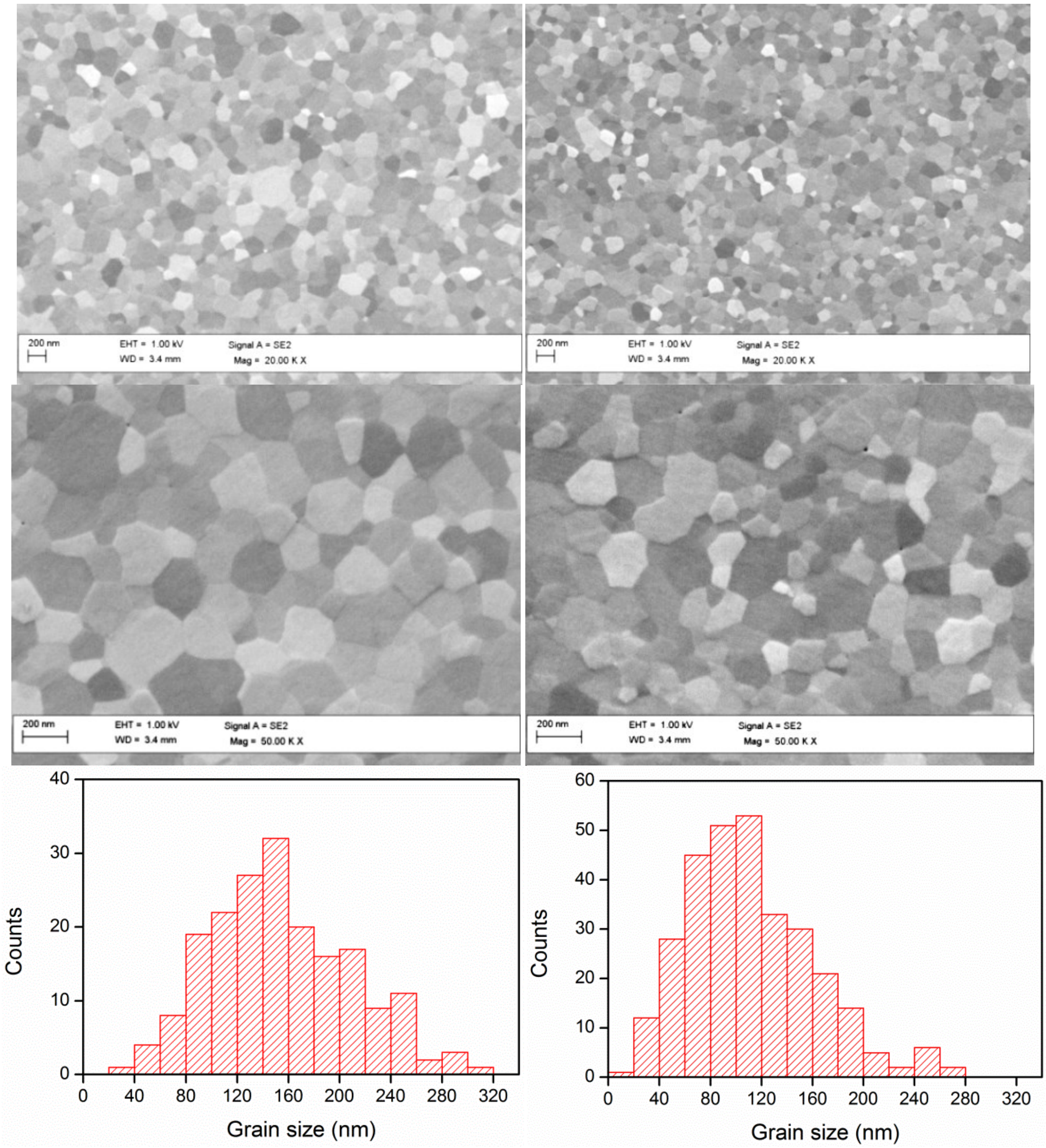

Figure S3. Samples with average grain size of left) 156 nm and right) 110 nm in two magnifications and with associated grain size distribution. Green bodies presented an apparent density of 47.7–48.5% T.D and were sintered at 1300–1350 °C for 2h.

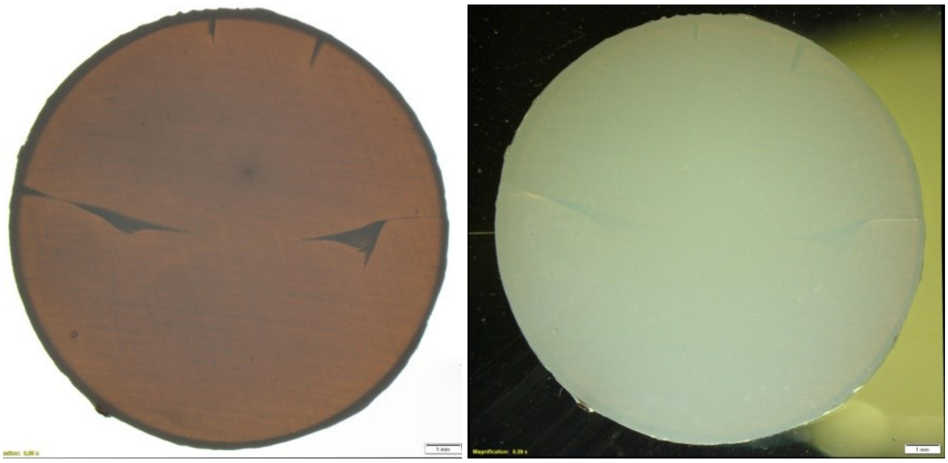

Figure S4. Representative image of samples that were cracked during sintering in a) transmission and b) reflection mode. Green bodies presented an apparent density of 52.6% T.D. and were sintered at 1150 °C for 2h.

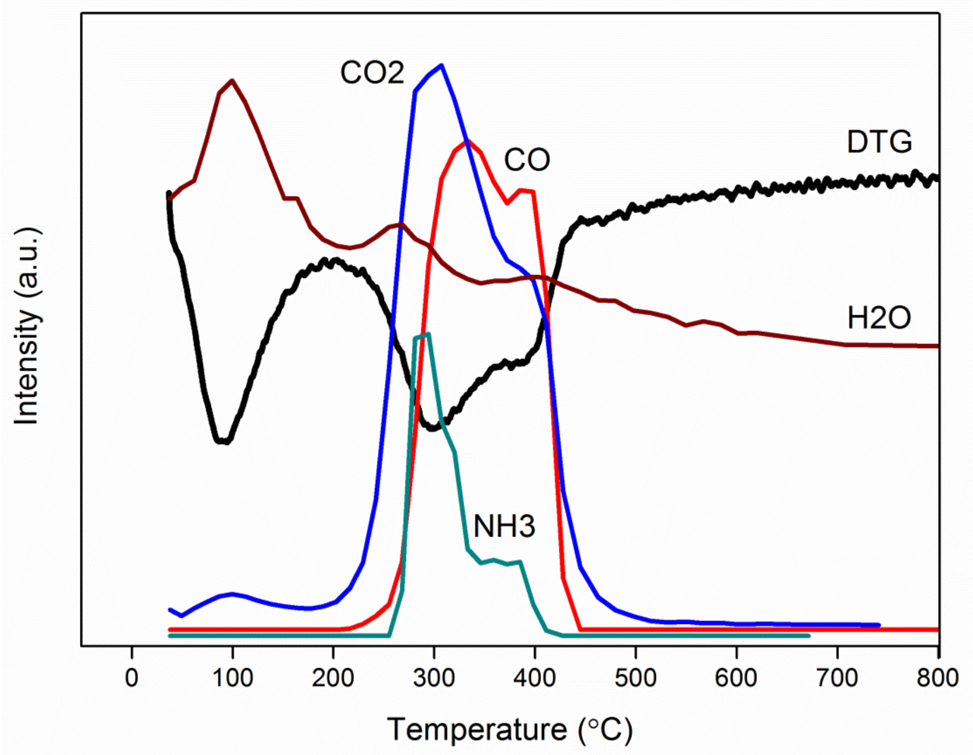

Figure S5. Results of µGC-TG on a green body of 3YSZ sample filtered at 20 bar and after drying (all curves are upward except DTG)

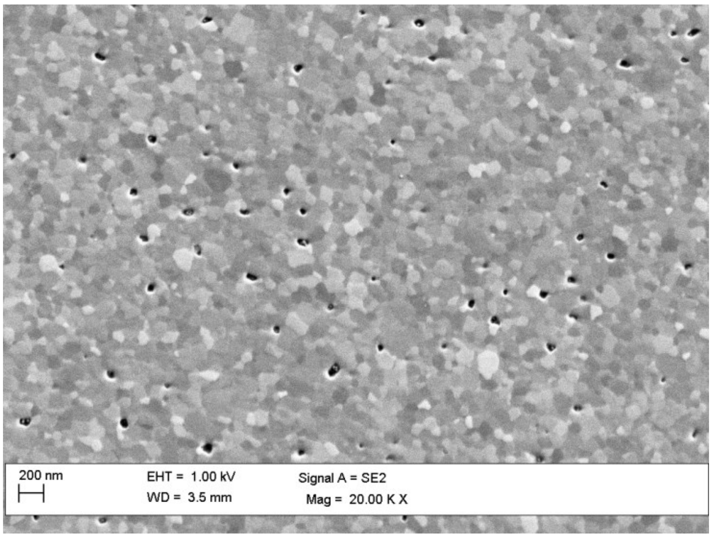

Figure S6. SEM image of a 3YSZ sample sintered at 950 °C showing formation of individual pores

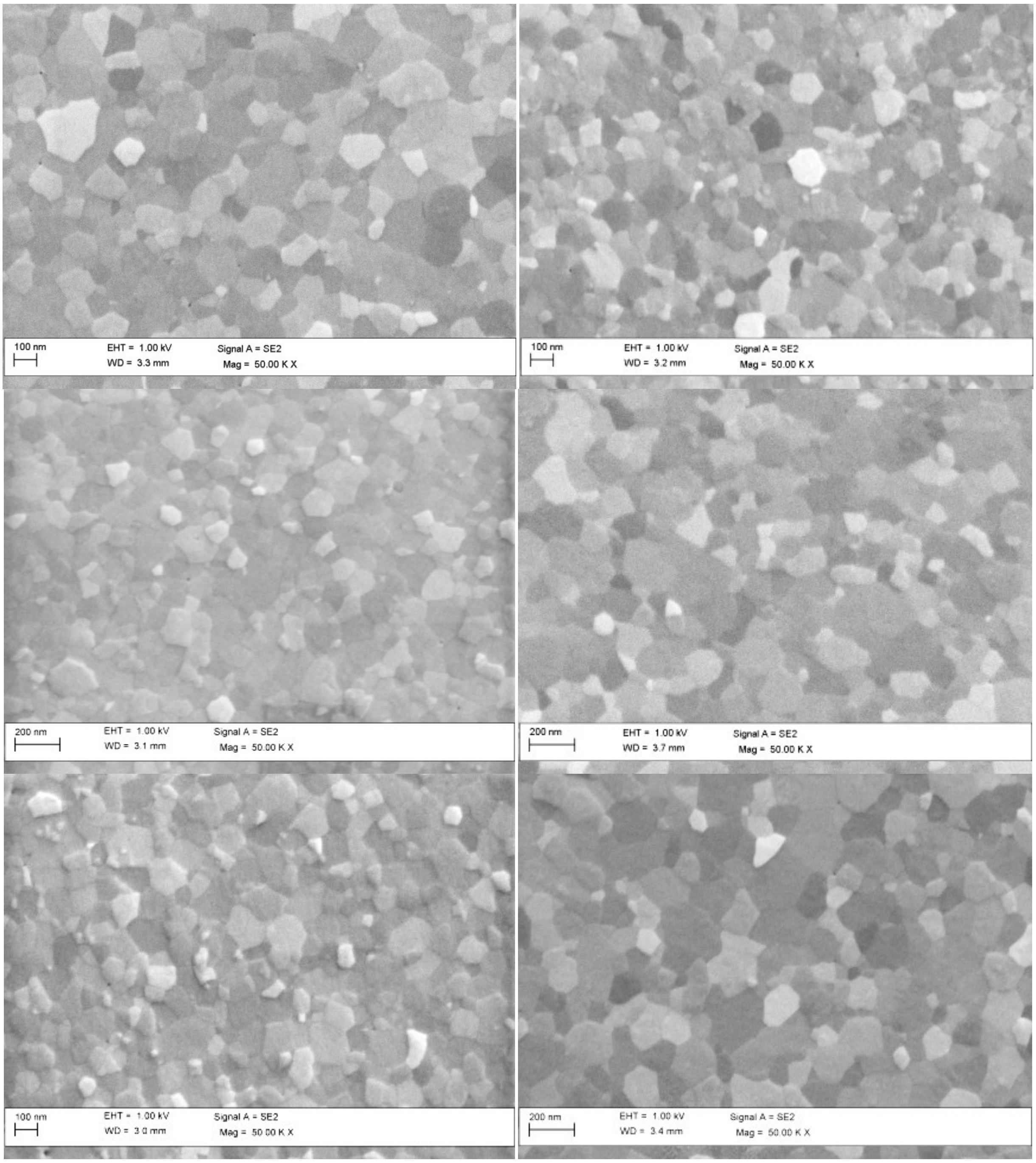

Figure S7. SEM of samples with different yttria contents from top to bottom; left) 1.5, 2, and 2.5YSZ and right) 4, 5, and 6YSZ

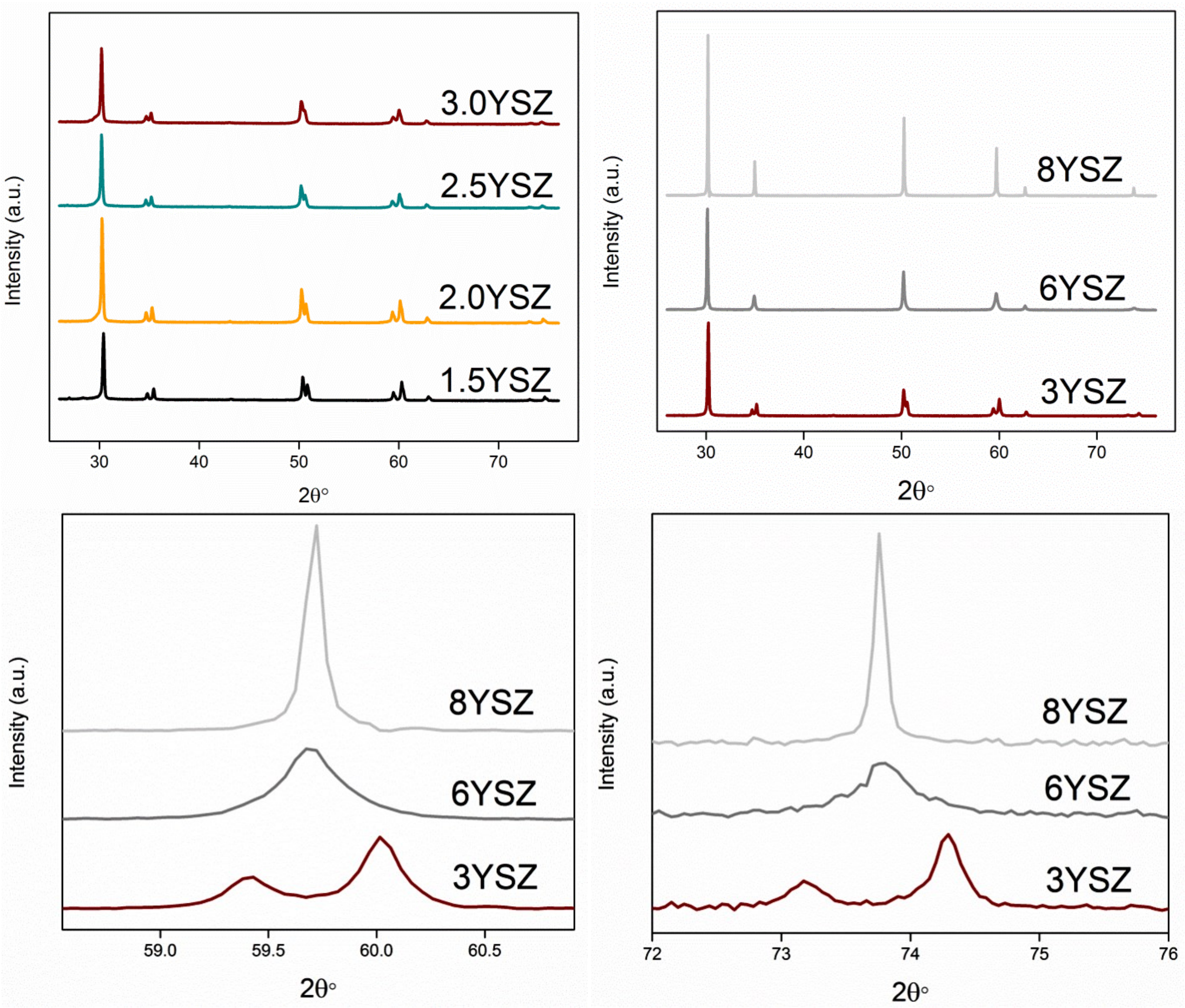

Figure S8. XRD pattern of YSZ samples top) with different yttria compositions and bottom) magnified at 2ϑ=59–61° and 2ϑ=72–76°

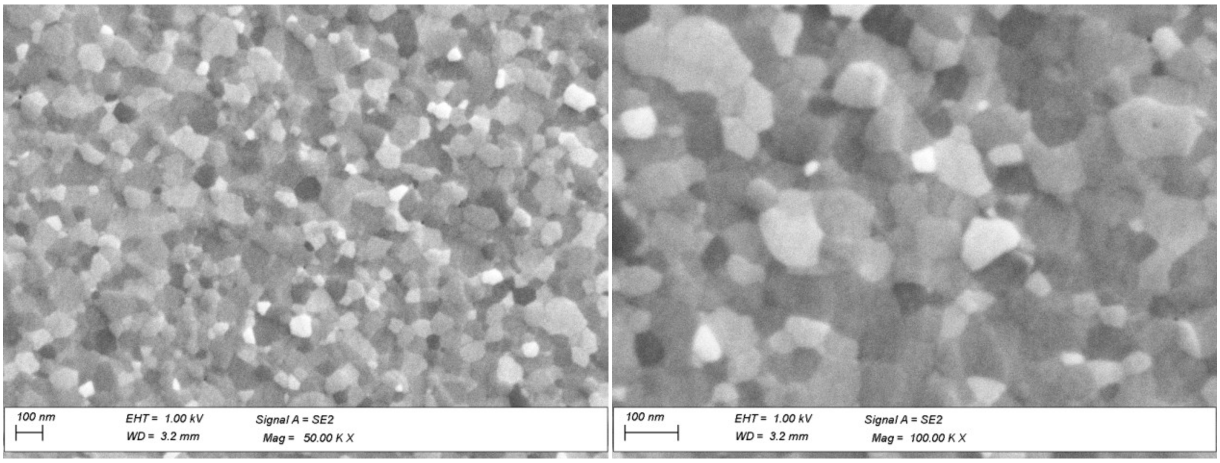

Figure S9. SEM images of HIP50 in different magnifications showing the average grain size of 50 nm

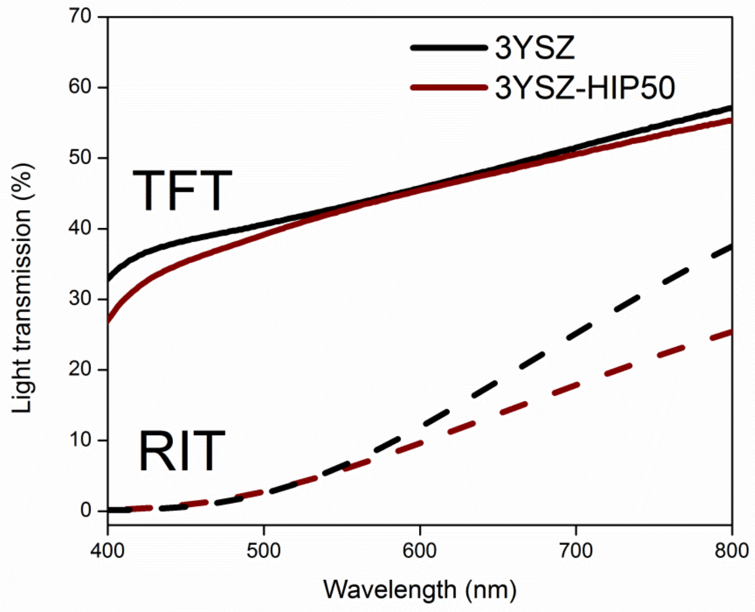

Figure S10. Comparison between light transmission of HIP50 after heat treatment in air and nanograin 3YSZ densified by conventional pressure-less sintering

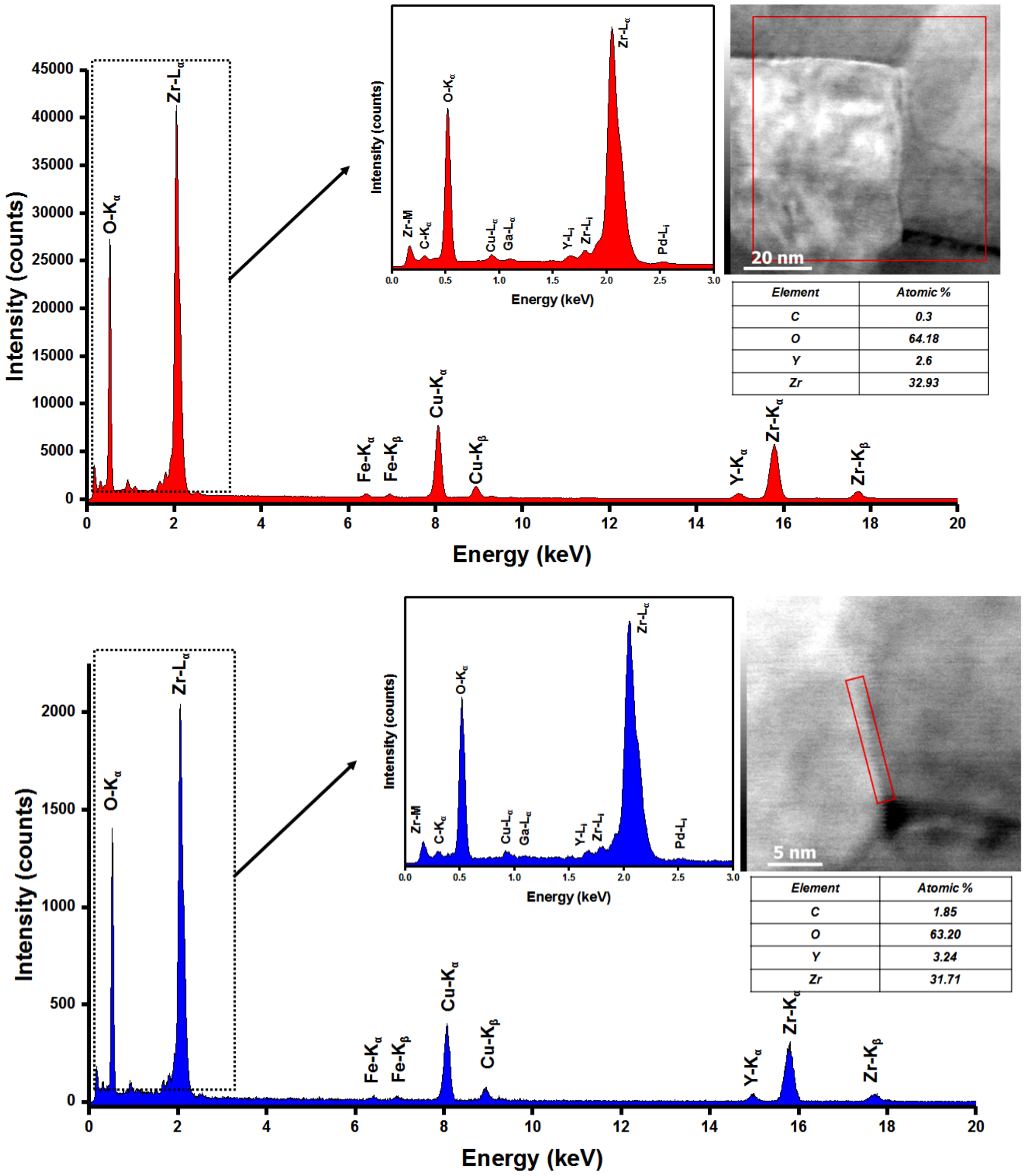

Element	*Atomic %*
C	*0.3*
O	*64.18*
Y	*2.6*
Zr	*32.93*

Element	*Atomic %*
C	*1.85*
O	*63.20*
Y	*3.24*
Zr	*31.71*

Figure S11. STEM-EDX elemental analysis of HIP50 after annealing air; top) overall region and bottom) grain boundary. Insets show the area of analysis.

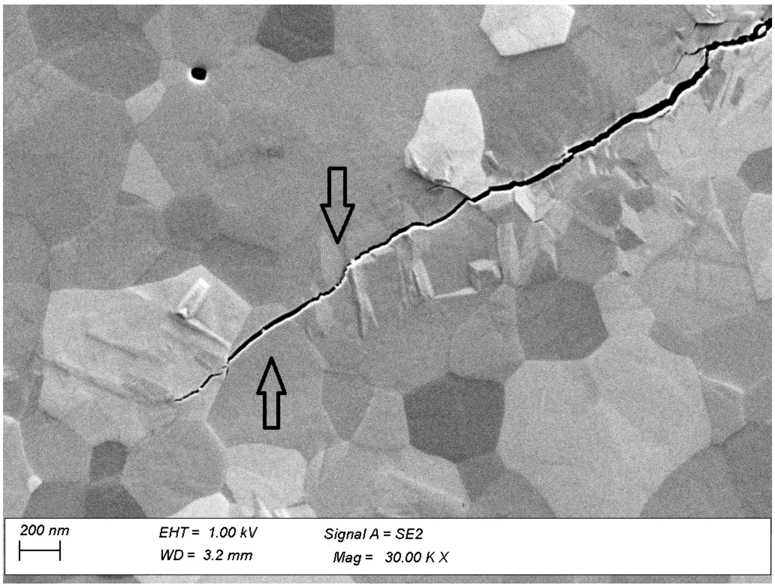

Figure S12. Vicinity of indentation cracks in 3YSZ with a grain size of 250 nm. Arrows show intergranular crack propagation in a grain without (left) and with (right) t→m transformation.

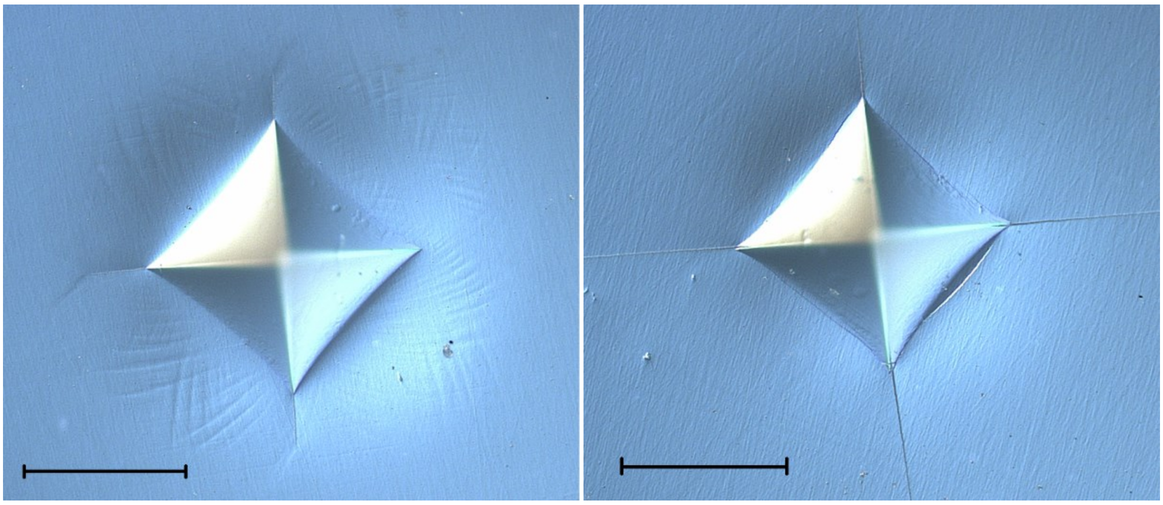

Figure S13. Optical images with polarized light from the vicinity of indents in left) 1.5 YSZ and right) 2YSZ. Scale bars show 100 µm. Lines of stress-induced phase transformation are visible as surface corrugation (transformation bands) in (left).

Table S1. Maximum volatile counts and associated temperatures in the µGC-TG test

Volatile	H_2O	CO_2	CO	NH_3
Maximum count	10400	4580	301	29
$T_{maximum\ count}$(°C)	99.6	307	333	294

Table S2. Representative ICP results of 3YSZ green body filtred at 20 bar and after drying

ZrO_2 (wt.%)	Y_2O_3 (wt.%)	HfO_2 (wt.%)	Fe_2O_3 (ppm)	Al_2O_3 (ppm)	SiO_2 (ppm)	CaO (ppm)	Na_2O (ppm)	Cr_2O_3 (ppm)	TiO_2 (ppm)
91.09	5.90	1.96	<5	<5	112	51	30	<5	<5

Table S3. Rietveld analysis of dense-YSZ ceramics with different yttria compositions

Material	Phase Name	wt.%	Yttria in phase (wt. %)	Total yttria (mol.%)	a (Å)	c (Å)	Rwp	R Bragg
1.5YSZ	Tetragonal	95.55	1.81	1.81	3.6011	5.1816	8.266	4.231
	Monoclinic	4.45						3.774
2YSZ	Tetragonal	100	2.27	2.27	3.6031	5.1793	11.235	2.07
3YSZ	Cubic	2.96	6.44	3.62	5.1280		9.938	2.26
	Tetragonal	97.04	3.60		3.6102	5.1716		2.13
5YSZ	Cubic	34.45	6.42	5.45	5.1354		9.102	1.77
	Tetragonal	65.55	4.94		3.6174	5.1638		2.60
6YSZ	Cubic	59.87	6.67	6.11	5.1363		9.109	2.00
	Tetragonal	40.13	5.26		3.6191	5.1619		2.81
8YSZ	Cubic	100	8.61	8.61	5.1433		12.394	5.55

Table S4. The results of quantitative analysis of interior grains and grain boundaries (GBs) by energy dispersive spectroscopyfor 3YSZ and HIP50 after annealing in air

Specimen		Elemental Distribution (at%)			
		C	O	Y	Zr
3YSZ	Interior	<0.01	52.9	3.2	43.9
	GBs	<0.01	51.8	3.6	44.6
HIP50	Interior	0.3	64.2	2.6	32.9
	GBs	1.8	63.2	3.3	31.7

Table S5. Light transmission and biaxial strength of nanograin zirconiain this work in comparison to micron grain-size commercial counterparts and YSZ synthesized by HIP/SPS

Sample	Grain size (nm)	RIT at 800 nm	Biaxial strength (MPa)
1.5YSZ	75±5	< 1%	2550
3YSZ		37%	1980
6YSZ		38%	730
8YSZ		51%	680
3YSZ(1)*	50	~25%	n.d.
3YSZ(2, 3)	430	n.d.	1200
3YSZ(2, 3)	333	n.d.	980
3YSZ(4)	230–290	n.d.	1250
3YSZ(4)	200–260	n.d.	1023–1220
3YSZ(6)**	75	33%	n.d.
3YSZ(7)	250–300	n.d.	650–997
3YSZ(8)*	470–840	< 1%	990–1400
3YSZ(9)	215–305	n.d.	604–730
5YSZ(7)	713	n.d.	485
5.5YSZ(2)	770	n.d.	410
5.5YSZ(3)	558	n.d.	539
8YSZ(1)*	50	~50%	n.d.
8YSZ(5)*	95	~48%	n.d.

(1) Advanced Functional Materials 17 (2007) 3267–3273
(2) Dental Materials 34 (2018) 879–890
(3) Journal of Dentistry 60 (2017) 70–76
(4) Journal of Prosthetic Dentistry 122 (2019) 396–403
(5) Journal of the American Ceramic Society 94 (2011) 2981–2986
(6) Journal of the American Ceramic Society 94 (2011) 1850–1858
(7) Dental Materials 32 (2016) 327–337
(8) Ceramics International 42 (2016) 1077–1085
(9) Acta Biomaterialia 16 (2015) 215–222
* Thickness of the sample for the light transmission test is 1 mm.
** Thickness of the sample for the light transmission test is 0.5 mm.